applied sciences

MDPI

Article

Rapid Online Solid-State Battery Diagnostics with Optically Pumped Magnetometers

Yinan Hu [1,2], Geoffrey Z. Iwata [1], Lykourgos Bougas [1], John W. Blanchard [2], Arne Wickenbrock [1,2], Gerhard Jakob [1], Stephan Schwarz [3], Clemens Schwarzinger [3], Alexej Jerschow [4,*] and Dmitry Budker [1,2,5]

1 Helmholtz-Institut Mainz, GSI Helmholtzzentrum für Schwerionenforschung, Johannes Gutenberg-Universität Mainz, 55128 Mainz, Germany; yinanhu1@uni-mainz.de (Y.H.); gziwata@gmail.com (G.Z.I.); lybougas@uni-mainz.de (L.B.); wickenbr@uni-mainz.de (A.W.); jakob@uni-mainz.de (G.J.); budker@uni-mainz.de (D.B.)
2 Helmholtz-Institut Mainz, GSI Helmholtzzentrum für Schwerionenforschung, 55128 Mainz, Germany; blanchard@uni-mainz.de
3 Institute for Chemical Technology of Organic Materials, Johannes Kepler University Linz, 4040 Linz, Austria; stephan.schwarz@jku.at (S.S.); Clemens.Schwarzinger@jku.at (C.S.)
4 Department of Chemistry, New York University, New York, NY 10003, USA
5 Department of Physics, University of California, Berkeley, CA 94720-7300, USA
* Correspondence: alexej.jerschow@nyu.edu

Received: 13 October 2020; Accepted: 3 November 2020; Published: 6 November 2020



Abstract: Solid-state battery technology is motivated by the desire to deliver flexible power storage in a safe and efficient manner. The increasingly widespread use of batteries from mass production facilities highlights the need for a rapid and sensitive diagnostic tool for identifying battery defects. We demonstrate the use of atomic magnetometry to measure the magnetic fields around miniature solid-state battery cells. These fields encode information about battery manufacturing defects, state of charge, and impurities, and they can provide important insights into battery aging processes. Compared with SQUID-based magnetometry, the availability of atomic magnetometers, however, highlights the possibility of constructing a low-cost, portable, and flexible implementation of battery quality control and characterization technology.

Keywords: rapid online diagnostics; atomic magnetometer; solid-state battery; magnetization; magnetic susceptibility

1. Introduction

Lithium-ion rechargeable batteries (LIBs) currently are considered the most promising secondary battery technology to power mobile devices, electric transportation, and power tools. Conventional LIBs typically employ liquid or gel-based electrolytes. These are often volatile and flammable, which gives rise to safety concerns [1,2]. Solid-state batteries incorporate ion conducting solid electrolytes instead, which avoid the issue of volatility and leakage. Among other things, solid electrolytes allow the use of electrode materials with high voltages (>5 V), because of their wider electrochemical window. Furthermore, the use of solid electrolytes could enable the use of lithium metal anodes, thereby providing a viable pathway for higher capacity devices, while maintaining the inherent safety of the battery [3]. Significant technological challenges need to be overcome to make solid-state-based LIBs a widespread reality, including, for example, the facilitation of fast ion transport and the establishment of good interfacial properties between electrodes and the electrolyte medium.

All these factors highlight the need for the development of advanced diagnostic methodology that would allow proper device characterization at different stages of a battery's life. Currently used

techniques which can give in situ/operando information include ultrasound diagnostics [4,5], synchrotron-based scanning transmission X-ray microscopy [6], X-ray micro-diffraction [7], and Raman spectroscopy [8]. Manufacturers typically perform electrochemical testing and limited 2D X-ray scanning [9,10]. X-ray tomography is another powerful (but costly) tool that is generally too slow for high-throughput use with commercial cells [9,11]. Ultrasound diagnostics are useful for characterization of cells based on changes in density and mechanical properties [12,13], but do not allow noncontact measurements, limiting their broad application.

Rapid techniques that can be used nondestructively are typically limited to electrical impedance spectroscopy, and lately, ultrasound techniques.

Recently, it was also demonstrated that magnetic susceptibility changes within cells could be measured nondestructively and without contact using an inside-out MRI (ioMRI) technique that used the ^{1}H nuclear spin resonance frequencies in water to measure the susceptibility-induced magnetic field changes surrounding a cell when placed in a strong magnetic field [14,15]. It was further shown that the changes in the magnetic susceptibility could be tracked across the charge–discharge cycle, and that these changes followed the expected trends of the lithiation state of the cathode material. This approach therefore provided a single-point state-of-charge measurement and allowed for the identification of inhomogeneities or non-idealities of charge storage in electrochemical cells [14]. Extensions of this method have been developed to encompass the characterization of electrical current distributions (operando) [16], robust imaging protocols in the presence of strong background magnetic fields or distortions [17,18], and a technique for mapping alternating magnetic fields produced by applied AC currents [19]. The latter approach is developed with the goal of providing a type of localized electrical impedance spectroscopy. It was further shown recently that ioMRI and an ultrafast inside-out NMR technique can be used to classify cells based on different types of defects [14,20].

Superconducting-quantum-interference-device (SQUID)-based magnetic properties measurement systems (MPMS) were used to demonstrate the relation between battery charge state and susceptibility in the lab [21–24]. An MPMS is usually used to measure the material susceptibility with high precision, and it contains two main parts: a SQUID magnetometer to measure the magnetic moment of the sample and a superconducting magnet to provide the background field. The MPMS used in this work fits well for material properties evaluation, but measurements are time-consuming and cannot be done with a full-size commercial cell due to the limitation of the sample size ($<(6 \times 6 \times 9\,\mathrm{mm}^3)$). In our experiments, we combine data from a commercial SQUID-based MPMS with data from a recently developed miniature atomic magnetometer battery scanner of our own design (see Figure 1).

Our previous work introduced a diagnostic method [25] based on atomic magnetometry. The measurement system contains a commercial zero-field rubidium vapor spin-exchange relaxation free magnetometer from QuSpin Inc. The system can achieve a temporal resolution of 150 Hz, and the spatial resolution of the magnetic field at the sensor is limited by the size of the atomic vapor cell, which is $3 \times 3 \times 3$ mm^3. The atomic magnetometer sensitivity is $15\,\mathrm{fT}/\sqrt{\mathrm{Hz}}$, in a frequency range from 1 to 150 Hz. The rationale for this approach was the possibility to use these sensitive devices ($\mathrm{pT}/\sqrt{\mathrm{Hz}}$ to $\mathrm{fT}/\sqrt{\mathrm{Hz}}$ sensitivity) to report on tiny magnetic field changes around cells as a function of charge state. Tested on Li-ion pouch cells, the measurements showed sensitivity to microampere-level transient internal currents and changes in the magnetic susceptibility of the battery depending on its charge state. The susceptibility measurements involved a long, flat solenoid piercing a magnetic shield, with magnetic field sensors placed outside the solenoid (see Figure 1). In this configuration, the sensor does not "see" the magnetic field of the long solenoid; however, it is fully sensitive to the induced field produced by the battery in the presence of the solenoid field.

Here, we extend the measurements to miniature commercial solid-state batteries (both operational and defective) and benchmark the atomic magnetometer results with those based on SQUIDs (Quantum Design MPMS-XL-5). The sensitivity of atomic magnetometers provides opportunities for device characterization to sense small differences in magnetic properties as a function of device history or state.

For these chip-based cells, in particular, overheating leads to loss of saturation magnetization; hence, it is easily identifiable in the measurements. The studies are further supported by inductively coupled plasma mass spectrometry (ICP-MS) in order to identify the composition of the cells under study and the origin of the magnetization in these measurements.

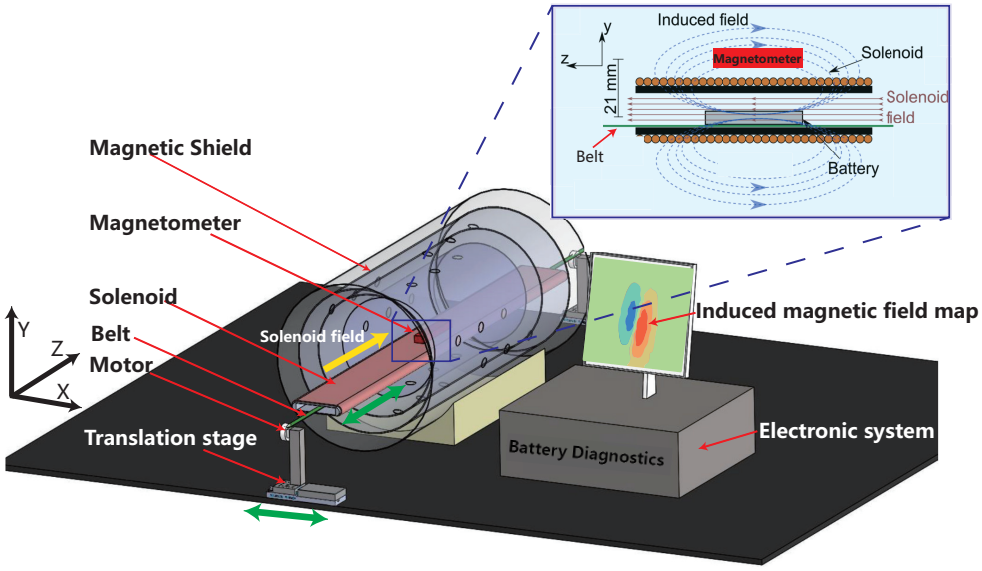


Figure 1. Experimental setup. A motor-driven conveyor belt moves the battery cell through a long solenoid, which can provide a constant background magnetic field. The magnetometer sensor is placed in the ultra-low-field region, above the solenoid, the solenoid is shown extending beyond the four-layer Twinleaf MS-2 magnetic shielding. The conveyor belt moves the battery back and forth along the z axis, while translation stages on each end move the entire belt with 0.1-mm precision along the x axis. (Inset) Side view of the experimental arrangement [25].

2. Results

The MPMS measurements show that the cells under study here produced stronger magnetic moments than the cells studied in the earlier work [25]. In addition to paramagnetic behavior, a dominating ferromagnetic behavior is observed (see Figure 2c; the grey area in the curve shows the variation between different battery cells). From the m-H curve, we can infer that our system behaves predominantly as a soft ferromagnetic material and contains a relatively narrow hysteresis loop in the low-field region (see inset).

An examination of ICP-MS results (see Table 1) indicates that a possible origin of the ferrormagnetic components is nickel metal. While nickel can also be a component of cathode materials, for typical cathodes, the amount identified is much lower than what would be needed to account for our observations—for example, for different types of nickel manganese cobalt oxide (NMC) materials [26]. The assumption that the saturation magnetization determined from SQUID magnetometry due to metallic nickel is supported by the amount of nickel measured by the ICP-MS method. The saturation magnetization of nickel is 58.57 $\pm$ 0.03 J/(T·kg) (=A·m^2/kg) [27] and the nickel-weight difference between cells is around 0.99 $\times 10^{-9}$ kg; therefore, we obtain an upper limit for the magnetic moment differences corresponding to 6×10^{-8} J/T in agreement with the experimental results (see Figure 2c).

Figure 2a shows MPMS measurements for a healthy cell and one that was overheated above its highest working temperature of 80 °C. As seen here, the m-H curves are indistinguishable. The inset shows that induced magnetic moment of the healthy battery at a background of $\mu_0 H = 40\,\mu$T is somewhat stronger than that of the broken battery.

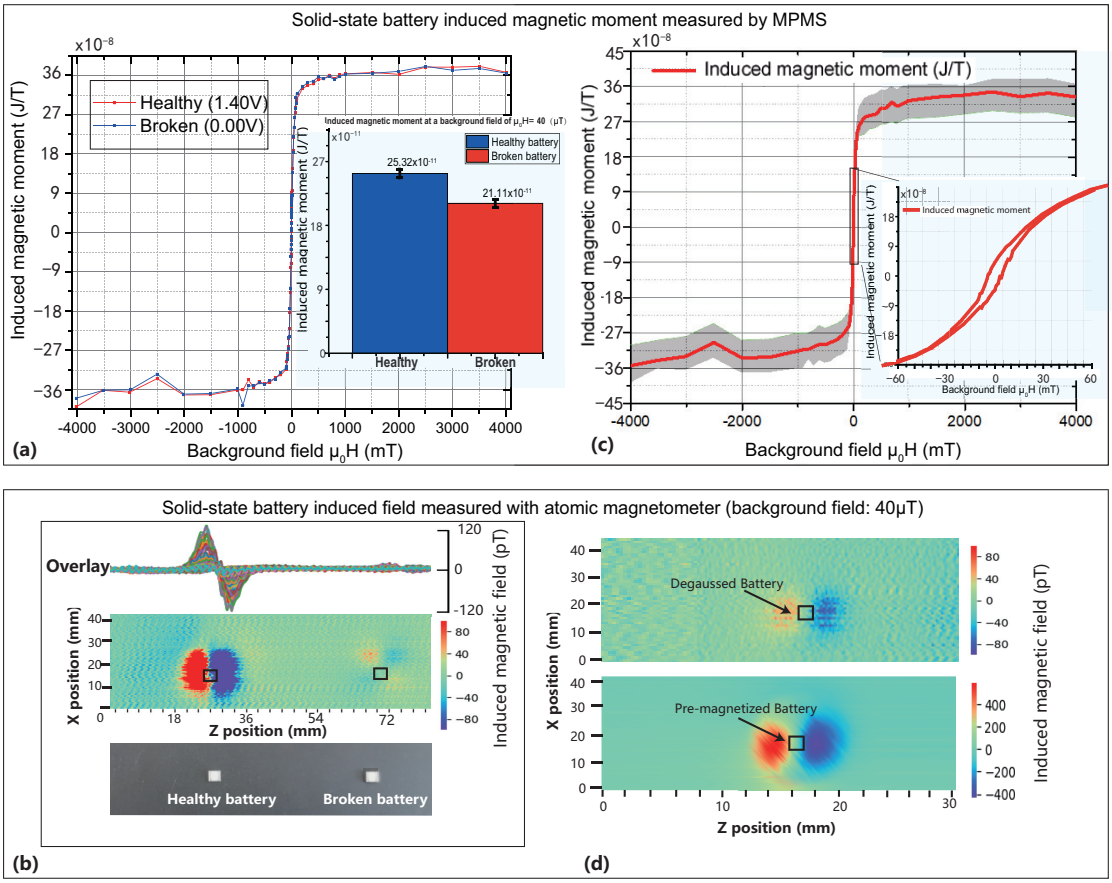


Figure 2. (**a**,**c**) Induced magnetic moment measurements using SQUID-based MPMS. (**b**,**d**) Induced magnetic field maps using the atomic magnetometer setup. (**a**,**b**) measurements of healthy and broken cells. The inset illustration in (**a**) shows the induced magnetic moment values scaled to a background magnetic field of $\mu_0 H = 40\,\mu$T. The grey area in (**c**) shows the variations between cell measurements using SQUID-based MPMS and the inset shows the hysteresis loop at small fields. The atomic magnetometer measurements in (**d**) show the induced magnetic field maps of a healthy cell after degaussing and magnetizing.

Table 1. Elemental content of the cell measured with inductively coupled plasma mass spectrometry. The mass of the cell is 0.045 g. Mn, Fe, and Co could not be detected above the detection threshold.

Element	Unit	Value
Li	mg/kg	12,685 ± 500
Mg	mg/kg	4
Al	mg/kg	417 ± 60
K	mg/kg	103 ± 9
Ca	mg/kg	24
V	mg/kg	27,889 ± 2000
Cr	mg/kg	42
Mn	mg/kg	—
Fe	mg/kg	—
Co	mg/kg	—
Ni	mg/kg	240 ± 22
Cu	mg/kg	188,628 ± 9000
Zn	mg/kg	271
Pb	mg/kg	6

Figure 2b shows the comparison of the measurements performed using the atomic magnetometer. For 40 different measured cells (20 healthy and 20 broken ones), the broken cells always showed a

different magnetic field pattern, and the induced field of broken batteries was weaker; the upper plot in this figure shows the overlaid data, the middle plot is the induced field map, and the bottom image shows that healthy and broken cells do not differ in their outward appearance.

In order to provide an independent verification for the origin of the magnetization that gives rise to the measurements, we performed these experiments by first pre-magnetizing the healthy cell with a 0.05 T magnet and comparing the measurement with one from a healthy cell that has undergone degaussing. The results indicate that the pre-magnetized healthy cells show similar values as the healthy cells measured, and the degaussed healthy cells show significantly reduced magnetization, similar to the broken (heated) cell (see Figure 2d).

3. Discussion

As the results show, our battery scanner could rapidly measure that the magnetization becomes weaker or stronger, depending on whether the cells are either degaussed or magnetized. In particular, these measurements allow one to immediately conclude that a cell has been overheated—for example, something that is of concern for chip-based devices.

MPMS is an ideal tool to study magnetic properties of materials, and is widely applied to battery prototype research [24]. It can evaluate the charge-state of the battery precisely by monitoring the transition metal's magnetic property during the charge or discharge period [21,28]. In this work, MPMS could provide a high background magnetic field (−4 to 4 T), giving access to the complete m-H curve [29], while our piercing solenoid system could only provide a stable background magnetic field from −80 to 80 µT. However, the superconducting coil of the MPMS suffers from residual magnetic field due to trapped flux, which is absent in our normal conducting coils that also allow for a much higher resolution of the background field. Therefore, our system is better suited for measurements at low fields in order to identify ferromagnetic contributions influenced by temperature [30] (see Figure 2b).

Furthermore, the atomic magnetometer setup could produce a diagnostic map of the battery cells' induced magnetic field within 20 s, providing potential resolution of the distribution of magnetic particles. A high-speed motor or a magnetometer array instead of a single sensor could even be used for these noncontact diagnostics of batteries on a sub-second time scale. These measurements can be performed in situ and operando with differently sized cells and under factory conditions. We show that batteries damaged by heating can be identified; this is particularly important for surface-mounted devices.

The magnetic field detection sensitivity of our setup is better than 400 fT/$\sqrt{\text{Hz}}$ from 1 to 150 Hz, which could help to detect a microgram difference in nickel content between cells. The dynamic range of our atomic magnetometer is approximately 5 nT, which also puts an upper limit on the nickel concentration. Recent developments in Earth-field atomic magnetometers with larger dynamic ranges [31] could solve this problem. These direct magnetic field measurements with atomic magnetometers provide hitherto inaccessible opportunities for cell characterization, classification, and monitoring in research and industry. Apart from battery diagnostics, the technique can be applied to general magnetic-susceptibility-based diagnostics, as well as for residual magnetization measurements—for example, in rock magnetism studies and magnetic materials testing [32].

4. Materials and Methods

4.1. Solid-State Battery Cells

All the measurements were performed on a commercially available all-ceramic solid-state battery (CeraCharge^{TM}), which is a rechargeable surface mount device (SMD) pictured in Figure 3a. The battery is designed as a chip-scale multi-layer passive component. It incorporates a Li-based ceramic solid electrolyte. The central copper electrode is used to collect electrons [see Figure 3b]. The capacity of the battery is 100 µAh at a rated voltage of 1.4 V.

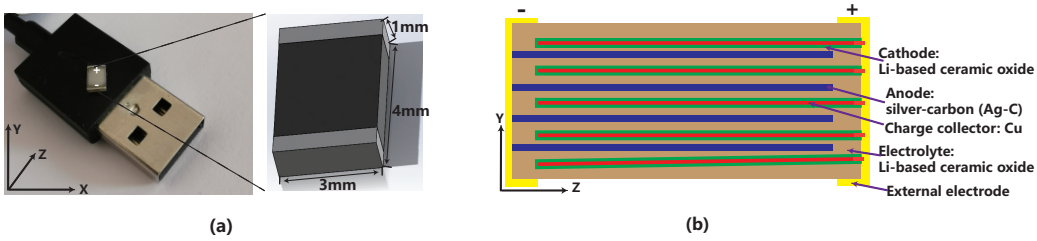


Figure 3. (**a**) Rechargeable solid-state battery (CeraCharge^{TM}) from TDK Corporation (www.tdk-electronics.tdk.com). (**b**) Z–Y cross-section view of the battery [33].

4.2. Measurement Apparatus

The measurements in our setup [25] were automated with the use of a conveyor belt moving the battery across the measurement region within a second. The belt moved the battery past the sensors for scanning along the z-coordinate. The cell was automatically translated along the x direction for the next scan while it was transported back to the original z position. Magnetic field maps recorded with the solenoid current turned on were consistent with maps expected for a rectangular block with approximately uniform susceptibility (similar to a dipole field), and the induced field could be calculated precisely by subtracting the magnetic field value with solenoid current turned off from the magnetic field value with the solenoid current turned on. All measurements in this work were carried out at room temperature.

4.3. Cell Preparation and Analyses

The cells are prepared in different states, which include healthy cells that can power devices (e.g., an LED), broken cells (that were heated to a high enough temperature such that the voltage after cooldown was close to zero, and that can no longer be recharged to a level where they can be used to power devices), and healthy cells demagnetized with a degaussing machine and magnetized with a permanent magnet with a field of 0.05 T applied for 20 s.

The SQUID magnetometry measurement was carried out with a commercial setup (Quantum Design MPMS-XL-5), and a gelatine capsule was used as a sample holder to position the cell.

For each ICP-MS measurement, two cells were microwave-digested in 4 mL HNO_3 at 210 °C. In order to dissolve further inorganic components, in a second step, the digestion was repeated with 1 mL HCl under the same conditions. The sample was subsequently diluted to 50 mL with 18 MOhm water. Low concentrations were measured from this solution and highly concentrated elements after 1:100 dilution with 1% HNO_3. ICP-MS measurements were performed using an XSeries 2, Thermo Scientific ICP-MS instrument.

5. Conclusions

We have examined here the possibility of using atomic magnetometers to characterize the magnetic properties of rechargeable solid-state Li-ion batteries in a rapid, nondestructive and noncontact fashion. The measurements are compared to SQUID-magnetometry-based measurements and supported by an elemental analysis. The magnetic components (nickel) in the cells are determined to be the source of the measured magnetization, and atomic magnetometry provides a convenient means of determining whether cells have been overheated. In a broader sense, atomic magnetometry provides sufficient sensitivity to sense the dependence of the magnetic susceptibility on the charge state and to identify certain defects or cell history. Given the difficulty of characterizing solid-state cells, such nondestructive and noncontact techniques could become useful tools in the analysis of cells at different stages of their life cycle.

Author Contributions: Conceptualization, Y.H., A.J., D.B. and G.Z.I.; methodology, A.J., G.Z.I., Y.H. and L.B.; software, Y.H.; validation, Y.H., G.J., S.S. and C.S.; formal analysis, Y.H.; investigation, D.B.; resources, A.W.; data curation, G.Z.I.; writing—original draft preparation, Y.H.; writing—review and editing, D.B., A.J. and S.S.; visualization, Y.H.; supervision, J.W.B., D.B., A.J. and L.B.; project administration, D.B.; funding acquisition, A.W. and D.B. All authors have read and agreed to the published version of the manuscript.

Funding: The work was funded in part by a grant by the U.S. National Science Foundation under award CBET 1804723 and the German Federal Ministry of Education and Research (BMBF) within the Quantumtechnologien program (FKZ13N14439).

Acknowledgments: We wish to thank the timely help given by TDK Corporation in providing the numbers of battery samples.

Conflicts of Interest: The authors declare no conflict of interest.

References

1. Li, M.; Lu, J.; Chen, Z.; Amine, K. 30 years of lithium-ion batteries. *Adv. Mater.* **2008**, *30*, 1800561. [CrossRef] [PubMed]
2. Goodenough, J.B.; Kim, Y. Challenges for rechargeable Li batteries. *Chem. Mater.* **2010**, *22*, 587–603. [CrossRef]
3. Kim, J.G.; Son, B.; Mukherjee, S.; Schuppert, N.; Bates, A.; Kwon, O.; Choi, M.J.; Chung, H.Y.; Park, S. A review of lithium and non-lithium based solid state batteries. *J. Power Sources* **2015**, *282*, 299–322. [CrossRef]
4. Robinson, J.B.; Maier, M.; Alster, G.; Compton, T.; Brett, D.J.; Shearing, P.R. Spatially resolved ultrasound diagnostics of Li-ion battery electrodes. *Phys. Chem. Chem. Phys.* **2019**, *21*, 6354–6361. [CrossRef] [PubMed]
5. Bauermann, L.P.; Mesquita, L.V.; Bischoff, C.; Drews, M.; Fitz, O.; Heuer, A.; Biro, D. Scanning acoustic microscopy as a non-destructive imaging tool to localize defects inside battery cells. *J. Power Sources Adv.* **2020**, *6*, 100035. [CrossRef]
6. Lim, J.; Li, Y.; Alsem, D.H.; So, H.; Lee, S.C.; Bai, P.; Cogswell, D.A.; Liu, X.; Jin, N.; Yu, Y.S.; et al. Origin and hysteresis of lithium compositional spatiodynamics within battery primary particles. *Science* **2016**, *353*, 566–571. [CrossRef] [PubMed]
7. Liu, J.; Kunz, M.; Chen, K.; Tamura, N.; Richardson, T. Visualization of Charge Distribution in a Lithium-Ion Battery Electrode. *Meet. Abstr.* **2010**, *2*, 208.
8. Panitz, J.C.; Novák, P.; Haas, O. Raman microscopy applied to rechargeable lithium-ion cells-Steps towards in situ Raman imaging with increased optical efficiency. *Appl. Spectrosc.* **2001**, *9*, 1131–1137. [CrossRef]
9. Wood, V. X-ray tomography for battery research and development. *Nat. Rev. Mater.* **2018**, *3*, 293–295. [CrossRef]
10. Väyrynen, A.; Salminen, J. Lithium ion battery production. *J. Chem. Thermodyn.* **2012**, *46*, 80–85. [CrossRef]
11. Yufit, V.; Shearing, P.; Hamilton, R.W.; Lee, P.D.; Wu, M.; Brandon, N.P. Investigation of lithium-ion polymer battery cell failure using X-ray computed tomography. *Electrochem. Commun.* **2011**, *13*, 608–610. [CrossRef]
12. Hsieh, A.G.; Bhadra, S.; Hertzberg, B.J.; Gjeltema, P.J.; Goy, A.; Fleischer, J.W.; Steingart, D.A. Electrochemical-acoustic time of flight: In operando correlation of physical dynamics with battery charge and health. *Energy Environ. Sci.* **2015**, *8*, 1569–1577. [CrossRef]
13. Davies, G.; Knehr, K.W.; Van Tassell, B.; Hodson, T.; Biswas, S.; Hsieh, A.G.; Steingart, D.A. State of charge and state of health estimation using electrochemical acoustic time of flight analysis. *J. Electrochem. Soc.* **2017**, *164*, A2746–A2755. [CrossRef]
14. Ilott, A.J.; Mohammadi, M.; Schauerman, C.M.; Ganter, M.J.; Jerschow, A. Rechargeable lithium-ion cell state of charge and defect detection by in-situ inside-out magnetic resonance imaging. *Nat. Commun.* **2018**, *9*, 1776. [CrossRef]
15. Ilott, A.J.; Mohammadi, M.; Chang, H.J.; Grey, C.P.; Jerschow, A. Real-time 3D imaging of microstructure growth in battery cells using indirect MRI. *Proc. Natl. Acad. Sci. USA* **2016**, *113*, 10779–10784. [CrossRef] [PubMed]
16. Mohammadi, M.; Silletta, E.V.; Ilott, A.J.; Jerschow, A. Diagnosing current distributions in batteries with magnetic resonance imaging. *J. Magn. Reson.* **2019**, *309*, 106601. [CrossRef]
17. Romanenko, K.; Jerschow, A. Distortion-free inside-out imaging for rapid diagnostics of rechargeable Li-ion cells. *Proc. Natl. Acad. Sci. USA* **2019**, *116*, 18783–18789. [CrossRef]

18. Romanenko, K.; Kuchel, P.W.; Jerschow, A. Jerschow Alexej, Accurate visualization of operating commercial batteries using specialized magnetic resonance imaging with magnetic field sensing. *Chem. Mater.* **2020**, *32*, 2107–2113. [CrossRef]
19. Benders, S.; Mohammadi, M.; Ganter, M.J.; Klug, C.A.; Jerschow, A. Mapping oscillating magnetic fields around rechargeable batteries. *J. Magn. Reson.* **2020**, *319*, 106811. [CrossRef]
20. Pigliapochi, R.; Benders, S.; Silletta, E.; Glazier, S.; Lee, E.; Dahn, J.; Jerschow, A. Ultrafast inside-out NMR assessment of Rechargeable Cells. *Batter. Supercaps* **2020**, *31*, 1022. [CrossRef]
21. Chernova, N.A.; Nolis, G.M.; Omenya, F.O.; Zhou, H.; Li, Z.; Whittingham, M.S. What can we learn about battery materials from their magnetic properties? *J. Mater. Chem.* **2011**, *21*, 9865–9875. [CrossRef]
22. Klinser, G.; Topolovec, S.; Krenn, H.; Würschum, R. Process Monitoring of Charging/Discharging of Lithium Ion Battery Cathodes by Operando SQUID Magnetometry. In *Encyclopedia of Interfacial Chemistry: Surface Science and Electrochemistry: Reference Module in Chemistry, Molecular Sciences and Chemical Engineering*; Wandelt, K., Ed.; Elsevier: Amsterdam, The Netherlands, 2018; pp. 849–855
23. Quantum Design, Inc. *MPMS Application Note 1014-213*; Quantum Design, Inc.: San Diego, CA, USA, 2002; Volume 21, pp. 10–20.
24. Klinser, G.; Topolovec, S.; Kren, H.; Koller, S.; Krenn, H.; Wurschum, R. Charging of lithium cobalt oxide battery cathodes studied by means of magnetometry. *Solid State Ion.* **2016**, *293*, 64–71. [CrossRef]
25. Hu, Y.; Iwata, G.Z.; Mohammadi, M.; Silletta, E.V.; Wickenbrock, A.; Blanchard, J.W.; Budker, D.; Jerschow, A. Sensitive magnetometry reveals inhomogeneities in charge storage and weak transient internal currents in Li-ion cells. *Proc. Natl. Acad. Sci. USA* **2020**, *117*, 10667–10672. [CrossRef] [PubMed]
26. Kaboli, S.; Demers, H.; Paolella, A.; Darwiche, A.; Dontigny, M.; Clement, D.; Guerfi, A.; Trudeau, M.L.; Goodenough, J.B.; Zaghib, K. Behavior of Solid Electrolyte in Li-Polymer Battery with NMC Cathode via in-Situ Scanning Electron Microscopy. *Nano Lett.* **2020**, *20*, 1607–1613. [CrossRef]
27. Danan, H.; Herr, A.; Meyer, A.J. New determinations of the saturation magnetization of nickel and iron. *J. Appl. Phys.* **1968**, *39*, 669–670. [CrossRef]
28. Klinser, G.; Topolovec, S.; Kren, H.; Koller, S.; Gössler, W.; Krenn, H.; Würschum, R. Continuous monitoring of the bulk oxidation states in $Li_xNi_{1/3}Mn_{1/3}Co_{1/3}O_2$ during charging and discharging. *Appl. Phys. Lett.* **2016**, *109*, 213901. [CrossRef]
29. Buchner, M.; Hofler, K.; Henne, B.; Ney, V.; Ney, A. Tutorial: Basic principles, limits of detection, and pitfalls of highly sensitive SQUID magnetometry for nanomagnetism and spintronics. *J. Appl. Phys.* **2018**, *124*, 161101. [CrossRef]
30. Coey, J.M. *Magnetism and Magnetic Materials*; Cambridge University Press: Cambridge, UK, 2010; Volume 124, pp. 128–194
31. Limes, M.E.; Foley, E.L.; Kornack, T.W.; Caliga, S.; McBride, S.; Braun, A.; Lee, W.; Lucivero, V.G.; Romalis, M.V. Portable magnetometry for detection of biomagnetism in ambient environments. *Phys. Rev. Appl.* **2020**, *14*, 011002. [CrossRef]
32. Dang, H.B.; Maloof, A.C.; Romalis, M.V. Romalis Michael V, Ultrahigh sensitivity magnetic field and magnetization measurements with an atomic magnetometer. *Appl. Phys. Lett.* **2010**, *979*, 151110. [CrossRef]
33. Rechargeable Solid-State SMD Battery for IoT Applications. 2018. Available online: www.tdk-electronics.tdk.com/en/2471330/tech-library/articles/applications---cases---video/rechargeable-solid-state-smd-battery-for-iot-applications/2431020 (accessed on 1 October 2020).

Publisher's Note: MDPI stays neutral with regard to jurisdictional claims in published maps and institutional affiliations.

© 2020 by the authors. Licensee MDPI, Basel, Switzerland. This article is an open access article distributed under the terms and conditions of the Creative Commons Attribution (CC BY) license (http://creativecommons.org/licenses/by/4.0/).